Journal of Materials Chemistry A

PAPER

View Article Online
View Journal | View Issue

Cite this: J. Mater. Chem. A, 2019, 7, 27576

Understanding three-dimensionally interconnected porous oxide-derived copper electrocatalyst for selective carbon dioxide reduction†

Thuy-Duong Nguyen-Phan, *[ab] Congjun Wang,[ab] Chris M. Marin,[ab] Yunyun Zhou,[a] Eli Stavitski,[c] Eric J. Popczun,[a] Yang Yu,[a] Wenqian Xu,[d] Bret H. Howard,[a] Mengling Y. Stuckman,[ab] Iradwikanari Waluyo,[c] Paul R. Ohodnicki Jr[a] and Douglas R. Kauffman *[a]

In this work, we have investigated a hierarchical CuO-derived inverse opal (CuO-IO) catalyst with high CO selectivity up to 80–90% and minimal H_2 evolution at moderate potentials for CO_2 electroreduction. The three-dimensionally (3D) structured, porous catalyst was composed of small CuO nanoparticles and exhibited a peak CO faradaic efficiency (FE) of 72.5% (±1.8), complete suppression of H_2 formation, and good stability over 24 hours operation at −0.6 V *versus* the reversible hydrogen electrode (RHE). *In situ* Raman, X-ray absorption spectroscopy and X-ray diffraction measurements indicated reduction of the catalyst into metallic Cu^0 oxidation state with dominant Cu(111) orientation under electrocatalytic conditions. We suggest that rapid depletion of CO_2 and protons at the highly roughened catalyst surface likely increased the local pH during the electrolysis. The combination of C_1 favoring Cu(111) surfaces and reduced local proton/CO_2 availability facilitated selective conversion of CO_2 into CO and reduced H_2 and C_2 products. Our work provides additional understanding of the structure–property relationships of 3D porous electrocatalysts for CO_2 reduction applications by evaluating the crystallographic orientation, oxidation state, and crystallite size of a CO-selective CuO-IO catalyst under realistic working conditions.

Received 13th September 2019
Accepted 22nd November 2019

DOI: 10.1039/c9ta10135g

rsc.li/materials-a

Introduction

Electrochemical CO_2 reduction (EC-CO_2RR) is a promising approach to convert CO_2 emissions into industrially-relevant and value-added chemicals and fuels.[1–7] However, due to slow kinetics and multi-electron transfer pathway, EC-CO_2RR usually requires significant overpotentials and can suffer from poor product selectivity and competitive hydrogen evolution reaction (HER). The development of highly active, selective and robust CO_2 conversion catalysts is of vital interest to overcome these drawbacks. The activity and selectivity towards specific products strongly depend on electrocatalyst morphology, surface roughness, nature of electrochemically active sites, electronic configuration, transport limitations, local pH environment at the electrode surface, *etc.*[2–18]

To date, numerous materials have been studied, including metals, oxides, and carbonaceous composites.[1–10] Expensive metals such as gold and silver can selectively convert CO_2 into CO,[4,6,19,20] which is a commodity chemical used in a variety of processes, including methanol and Fischer–Tropsch synthesis.[21,22] Copper-derived materials have also attracted much attention due to their low cost, high abundance, and ability to produce hydrocarbons or oxygenated hydrocarbons,[2,8–18,23–29] and efforts have recently focused on structural control to improve their product selectivity. A number of different structures and dimensions of copper-based catalysts have been investigated, such as nanoparticles, nanofoams, nanowires, prisms, dendrites, *etc.*[9–18,23–30] CuO-derived hierarchical nanostructures composed of nanowires exhibited

[a]National Energy Technology Laboratory, 626 Cochrans Mill Road, P.O. Box 10940, Pittsburgh, PA 15236-0940, USA. E-mail: ThuyDuong.NguyenPhan@netl.doe.gov; Douglas.Kauffman@netl.doe.gov

[b]Leidos Research Support Team, 626 Cochrans Mill Road, P.O. Box 10940, Pittsburgh, PA 15236-0940, USA

[c]Photon Sciences Division, National Synchrotron Light Source II, Brookhaven National Laboratory, Upton, New York 11973, USA

[d]X-ray Science Division, Advanced Photon Source, Argonne National Laboratory, Argonne, Illinois 60439, USA

† Electronic supplementary information (ESI) available: Includes detailed experimental methods; materials characterizations; calculation of faradaic efficiency; determination of electrochemical surface area and roughness factor; setup of *in situ* experiments; *ex situ* SEM, HR-TEM, EDX, XPS, SXRD, Raman, soft XAS data; chronoamperometric profiles, faradaic efficiencies, selectivities, total current densities, CO partial current densities, loading dependence performance; post-reaction XPS data; Tafel plots; control experiments; double layer capacitance plot; pore size comparison; *in situ* Raman, XANES, EXAFS, SXRD data; gas and ion chromatography spectra; and five ESI tables. See DOI: 10.1039/c9ta10135g

selective CO and HCOOH production with a total FE of 82.5% at −0.55 V *vs.* RHE that was attributed to the 3D porous structure of catalysts.[29] Mesoporous Cu_2O-derived foams were also found to selectively produce C_2H_4 and C_2H_6 with a maximum C_2 FE reaching 55% at −0.9 V *vs.* RHE due to the presence of dominant (100) surface sites for C–C coupling and temporal trapping of gaseous intermediates inside the mesopores.[30] Despite this progress, it is still challenging to fully understand the nature of electrochemically active sites because the product selectivity of copper catalysts strongly depends on their structure, morphology, and oxidation state.[10–15,18,24,31]

Inverse opal (IO) materials have been widely studied for applications in catalysis, photonics, photovoltaic devices, energy conversion, and energy storage.[31] The three-dimensional (3D) interconnected, highly porous structure of IOs are arranged in hexagonal close packed framework, offering large surface area and better adsorbability of reactant molecules.[26,27,31,32] Despite these benefits, only few studies on IO catalysts for EC-CO_2RR have been reported.[4,6,26,27,31] Porous mesostructured Au and Ag IO catalysts have shown improved CO selectivity due to the generation of pH gradients that reduced proton availability at the catalyst surface and suppressed competitive H_2 evolution.[4,6] Zhang and coworkers[26] found improved CO selectivity (∼45%) for cube-like Cu-IO, but the oxidation state and crystallographic orientation during EC-CO_2RR were not investigated. However, larger IO pore size significantly decreases CO FE while enhancing H_2 and C_2 formation.[26,27]

Substantial efforts have been devoted to characterizing Cu-based electrocatalysts during EC-CO_2RR working conditions;[8,12,15,17,18,31] however, *in situ* investigations of C_1 selective Cu-IO-based catalysts are still needed to understand their enhanced selectivity. Here, we investigate the performance of a hierarchical oxide-derived copper inverse opal (CuO-IO) catalyst that is constructed from ∼15 nm Cu-oxide nanoparticles arranged in a 3D porous framework. The catalyst demonstrated impressive CO selectivity and strong suppression of H_2 evolution over a wide potential window, achieving a peak FE of 72.5% (±1.8) at −0.6 V *vs.* RHE, and demonstrating good 24 hour durability. *In situ* characterization techniques, including Raman, X-ray absorption spectroscopy (XAS), and synchrotron X-ray diffraction (SXRD) under working conditions showed that the catalyst reduced to metallic Cu^0 with a dominant (111) surface under electrocatalytic conditions. We attribute the high C_1 selectivity and suppressed HER to a combination of the dominant presence of a Cu(111) surface[8,9,11] and a high local pH depleting the local concentration of protons available for H_2 production. This work provides additional insight into the catalytic-activity of copper-based IO catalysts, and further demonstrates that catalyst morphology can function as a catalyst design principle for selective CO_2 conversion.

Experimental

Synthesis of as-prepared hierarchical CuO inverse opal

All chemicals were purchased from Sigma-Aldrich and used as received without further purification. Hierarchical CuO inverse opal materials were prepared by infiltration of copper precursor solution with poly (methyl methacrylate) (PMMA) opal film (see ESI† for synthesis detail of PMMA latex and opal template). 20 μL of copper precursor solution including 0.625 g of copper(II) nitrate trihydrate ($Cu(NO_3)_2 \cdot 3H_2O$), 0.375 g of citric acid monohydrate ($C_6H_8O_7 \cdot H_2O$), and 10 mL of absolute ethanol (C_2H_5OH, 200 proof) was penetrated slowly into 10°-tilted PMMA opal and naturally evaporated overnight. The infiltrated film was subsequently annealed in air at 400 °C with ramping rate of 1 °C min^{-1} for 4 h to completely remove PMMA and reassemble hierarchical CuO inverse opal (namely CuO-IO) as a negative replica of bare PMMA opal.

Electrochemical CO_2 reduction measurement

Electrochemical CO_2 reduction experiments were carried out in a gas-tight, two-compartment H-cell separated by a Nafion 117 proton exchange membrane. Each compartment was filled with 50 mL of aqueous 0.1 M $KHCO_3$ electrolyte (99.99%, Sigma-Aldrich) and contained 100 mL headspace. Here ultra-pure deionized water (DIW) with 18.3 MΩ cm^{-1} resistivity (Barnstead EASYpure LF) was used in all electrochemical experiments to minimize the effect of any trace metal impurities from water on the EC-CO_2RR performance.[33,34] The catholyte was continuously purged with CO_2 (99.999%, Butler gas) at a flow rate of 20 mL min^{-1} (pH ∼6.8) during the experiments and stirred at 200 rpm. The counter and reference electrodes were Pt wire and Ag/AgCl (saturated NaCl, BASi®), respectively. The catalyst ink was prepared by dispersing 4 mg of as-prepared CuO-IO (scraped down from the glass substrates) in 200 μL of methanol and 10 μL of Nafion® 117 solution binder (Sigma-Aldrich, 5%). Working electrodes were fabricated by drop-casting the prepared ink onto PTFE-coated carbon paper gas diffusion layer (Toray paper 060, Alfa Aesar). The as prepared CuO-IO loading on carbon paper was kept at 2.8 ± 0.1 mg cm_{geo}^{-2} (based on geometric area) unless otherwise noted.

CO_2 reduction experiments were performed at ambient temperature and pressure using a SP-300 potentiostat (BioLogic Science Instrument). All potentials were referenced against the reversible hydrogen electrode (RHE) and the uncompensated resistance was automatically corrected at 85% (iR-correction) using the instrument software.[9,11,12,14] Typical working electrode resistances were 30–40 Ω. Short-term chronoamperometric experiments were conducted for 30 min at each applied potential sequentially between −0.2 V and −1.2 V *vs.* RHE. Long-term chronoamperometric experiments were conducted for 24 hours at −0.6 V *vs.* RHE. The total and partial current densities were normalized to the exposed geometric area. Each data point is an average of at least three independent experiments on different fresh electrodes. The evolved gas products were quantified by PerkinElmer Clarus 600GC equipped with both FID and TCD detectors, using ShinCarbon ST 80/100 Column and He as a carrier gas. The GC was calibrated regularly using a calibration mixture of gases with known composition. The liquid products in the catholytes were determined by Dionex ICS-5000+ ion chromatography using ED_{50} conductometric detector, ASRS suppressor in auto-generation mode,

AS11-HC column and KOH eluent with a gradient of 0.4–30 mM in 45 min run. The calculation of faradaic efficiency for each product is described in the ESI.†

Materials characterizations

Scanning electron microscopy (SEM) imaging was performed on a FEI Quanta 600F microscope operated at 10–20 kV equipped with an energy-dispersive X-ray (EDX) detector. High-resolution transmission electron microscopy (HR-TEM) and EDX analysis were carried out on a FEI Titan G2 80–300 kV operated at accelerating voltage of 300 kV. The CuO-IO sample was scraped down from the glass substrates, suspended in ethanol, drop-casted onto a holey carbon support Au grid, and naturally dried in air.

In situ Raman spectroscopy during EC-CO_2RR was performed on a Horiba LabRam HR-Evolution spectrometer with 785 nm laser as excitation source, a 10× long working distance objective, and a custom-made Teflon cell with a quartz window. 5 μL of the catalyst ink, composed of CuO-IO, Nafion and methanol, was drop-cast onto a glassy carbon working electrode. A Pt wire and Ag/AgCl were used as counter and reference electrodes, and iR-correction was applied in all measurements. 5 mL of 0.1 M $KHCO_3$ was continuously purged with CO_2 during the measurements and sequential Raman spectra were collected at various constant applied potentials. *Ex situ* measurement of fresh and post-reaction electrodes were recorded with 633 nm laser source and 100× working distance objective.

Hard X-ray absorption spectroscopy (XAS) characterization was performed at the 8-ID (ISS) beamline of the National Synchrotron Light Source II (NSLS-II) at Brookhaven National Laboratory. *In situ* Cu K-edge XAS experiments during CO_2 electrolysis were carried out using a custom-made polycarbonate cell which consisted of three interconnected chambers for working, Ag/AgCl reference, and Pt wire counter electrodes. A Kapton window in the working electrode chamber allowed the passage of X-rays (Fig. S1, ESI†). The cell was filled with 7 mL of aqueous 0.1 M $KHCO_3$ electrolyte and saturated with CO_2 gas using a constant flow rate of 10 mL min^{-1}. The fabrication of the CuO-IO working electrode was identical to the electrochemical measurement in H-cell, although the *in situ* cell was an open design and not gas tight. *In situ* Cu K-edge XAS spectra were collected using a Passivated Implanted Planar Silicon detector during the application of various cathodic potentials (*vs.* RHE, iR-corrected). Cu foil was used for energy calibration. Reference samples, including bulk Cu_2O and CuO powders, were diluted with boron nitride and pressed into pellets for *ex situ* measurement. These materials were also collected for energy normalization (at 8979 eV) and model fitting for X-ray absorption near-edge structure (XANES) and extended X-ray absorption fine structure (EXAFS) data processing. All Cu K-edge data were collected in fluorescence modes and subsequently analyzed using IFEFFIT freeware package.[35]

Synchrotron X-ray diffraction (SXRD) measurements were conducted at beamline 17-BM-B ($\lambda = 0.24136$ Å, 51.4 keV) of the Advanced Photon Source at Argonne National Laboratory. *Ex situ* SXRD analysis of powder samples was conducted by loading samples into Kapton capillaries, and two-dimensional diffraction patterns were collected by a PerkinElmer amorphous silicon detector. The *in situ* SXRD cell and experimental conditions were identical to those used for *in situ* XAS experiments, and SXRD patterns were collected during the application of cathodic potentials. The data acquisition was performed with QXRD and the diffraction ring was integrated using GSAS-II package.[36] The instrument parameters were calibrated using a Si standard; the phase determination and compositional fraction were subsequently determined by Rietveld refinement using GSAS-II.

Results

Materials characterizations

The electron microscopy images in Fig. 1A and S2–S4 (ESI†) show a three-dimensional interconnected backbone of as-prepared CuO-IO with an average cavity size of 180 ± 5 nm. The HR-TEM micrograph in Fig. 1B reveals the CuO-IO structure is composed of 15–20 nm CuO nanoparticles with lattice spacings of 0.272 nm, 0.252 nm, and 0.232 nm that can be indexed to (110), (002), and (200) planes of polycrystalline CuO, respectively.

The synchrotron XRD pattern of CuO-IO in Fig. 1C displays several diffraction peaks representative of monoclinic CuO (space group $C2/c$) with lattice constants $a = 4.7119$ Å, $b = 3.4350$ Å, $c = 5.1164$ Å. Neither cuprite Cu_2O nor metallic copper phases were found, and the mean CuO crystallite size of *ca.* 15 nm closely matched particle sizes determined from HR-TEM imaging. Cu K-edge XANES spectra (Fig. 1D) reveal that the line shape, and the positions of pre-edge (1s → 3d transition, at 8977 eV), shakedown feature (1s → 4p transition, at 8986 eV) and white line (at 8998 eV) for CuO-IO resemble the CuO standard, indicating Cu^{2+} oxidation state. Two maxima centered at 1.53 and 2.52 Å in corresponding Fourier transformed k^2-weighted EXAFS spectrum (Fig. S5, ESI†) are ascribed to Cu–O bond in the nearest neighbor shell and Cu–Cu in the next near neighbor coordination, respectively.[14,15] Additional XPS, Auger and Cu L-edge XAS data in Fig. S6 (ESI†) also confirmed the presence of CuO.

Electrochemical performance

The CO_2 electroreduction activity of as-prepared CuO-IO was evaluated using chronoamperometry between −0.2 V and −1.2 V *vs.* RHE as shown in Fig. 2A. Impressive C_1 selectivity was demonstrated over an extremely wide potential range, with only minor C_2H_4 (<5%) and H_2 between −0.9 V and −1.2 V and trace ethane −1.2 V (<0.1% FE) (Table S1, ESI†). Total geometric current densities of CuO-HIO catalyst were comparable to other oxide-derived copper electrocatalysts (Fig. S8, ESI†), but the C_1 product selectivity was much higher than expected for copper-based catalysts.[8–10,12–14,23,26,27] Methane and formic acid were the dominant products below −0.4 V, while CO production increased to a maximum faradaic efficiency (FE) of 72.5% at −0.6 V and maximum CO selectivity up to nearly 90% was observed between −0.7 V and −0.8 V

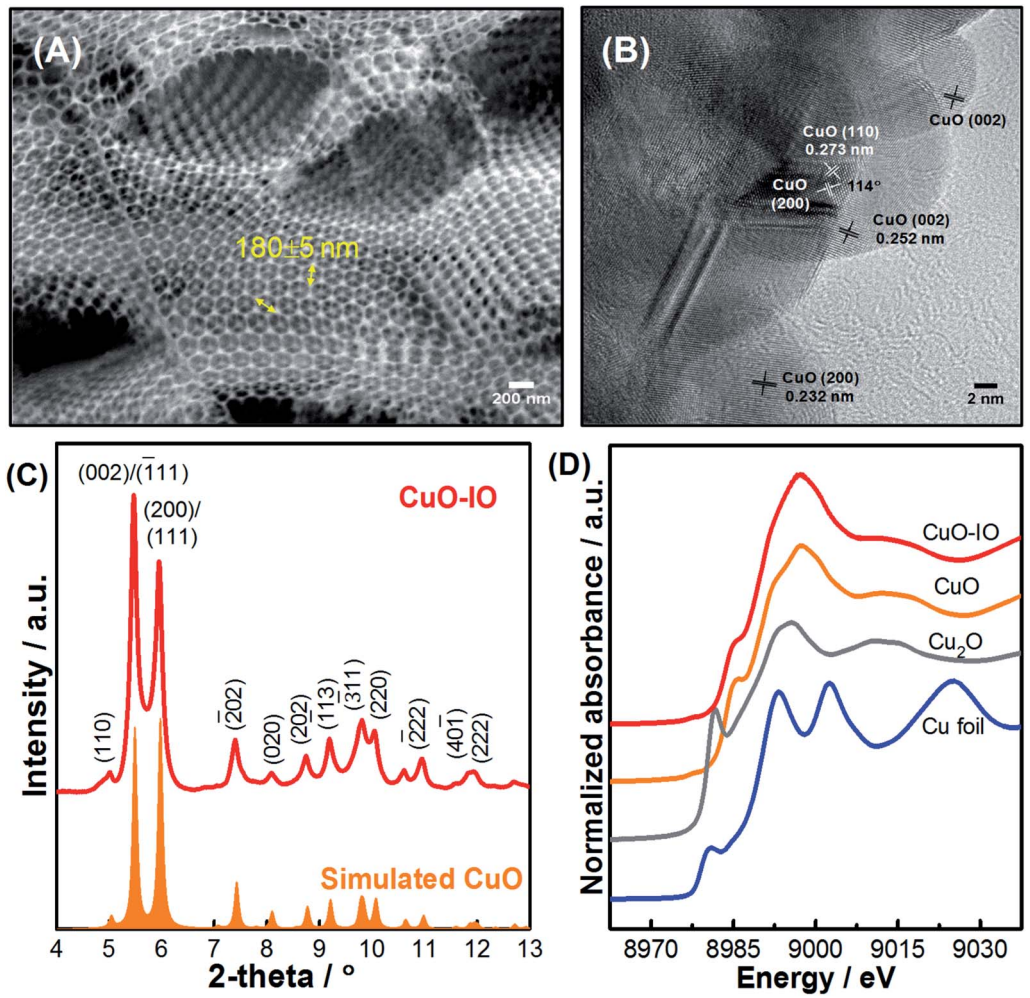

Fig. 1 (A) SEM image, (B) HR-TEM micrograph, (C) SXRD pattern (orange pattern is for simulated CuO), and (D) XANES Cu K-edge of as prepared CuO-IO. Orange, gray and blue spectra in (D) are bulk CuO, bulk Cu_2O and Cu foil standards.

(Fig. S9, ESI†). We point out that some potentials had less than 100% FE, which may stem from some fraction of the current going to copper oxide reduction and/or the production of liquid products that were either below the detection limit or not detectable by ion chromatography (Fig. S10, ESI†). Nevertheless, we observed an average C_1 FE of 78 ± 2% was observed between −0.2 to −1.1 V *vs.* RHE (Fig. S11, ESI†), which decreased to approximately 60% at −1.2 V *vs.* RHE due to the increased HER at large overpotentials. The CO yield strongly increased from ~30 $\mu mol_{CO}\ g_{catalyst}^{-1}\ h^{-1}$ at −0.2 V to 60–70 $mmol_{CO}\ g_{catalyst}^{-1}\ h^{-1}$ at potentials more negative than −1.0 V (Table S1, ESI†).

Control experiments with different CuO-IO catalyst loadings, varied catalyst layer thickness, and a graphite counter electrode produced similarly high CO selectivities (Fig. S12 and S13, ESI†), which rules out a strong loading-dependence or unintentional contamination from the Pt counter electrode impacting the measured product distribution.[37] Finally, the bare carbon paper demonstrated almost exclusive H_2 production with only trace CO and CH_4 detected from −0.7 V to −1.2 V (Fig. S14, ESI†).

Long-term CO_2 electrolysis demonstrated consistent CO selectivity for the CuO-IO catalyst. As shown in Fig. 2B, an average 67 ± 2% CO FE was found over 24 hours at −0.6 V with a stable current density of *ca.* 2.5 mA cm^{-2} and no detectable H_2 evolution (Fig. S15, ESI†). Pt crossover through Nafion membrane or deposition of other trace metal impurities from water can impact catalyst activity and stability.[33,34] XPS analysis of post-reaction electrodes after long-term runs at −0.6 V using Pt wire and graphite counter electrodes ruled out significant deposition of trace Pt, Zn, Pb or Fe elements onto the electrode surface (Fig. S16, ESI†). Post reaction electron microscopy in Fig. S17 (ESI†) revealed the catalyst preserved its general inverse opal structure. The sustained CO selectivity and current density over 24 hour operation indicates the CuO-IO catalyst is a robust CO_2-to-CO conversion catalyst.

For comparison, we also tested the EC-CO_2RR performance of commercially-available bulk CuO powder (~1–5 μm) and non-IO, ~50 nm diameter CuO nanoparticles (NPs) with similar catalyst loading. The morphology, crystallographic orientation and oxidation state of these oxide materials were determined by SEM, SXRD and XAS measurements (Tables S2, S3 and Fig. S18,

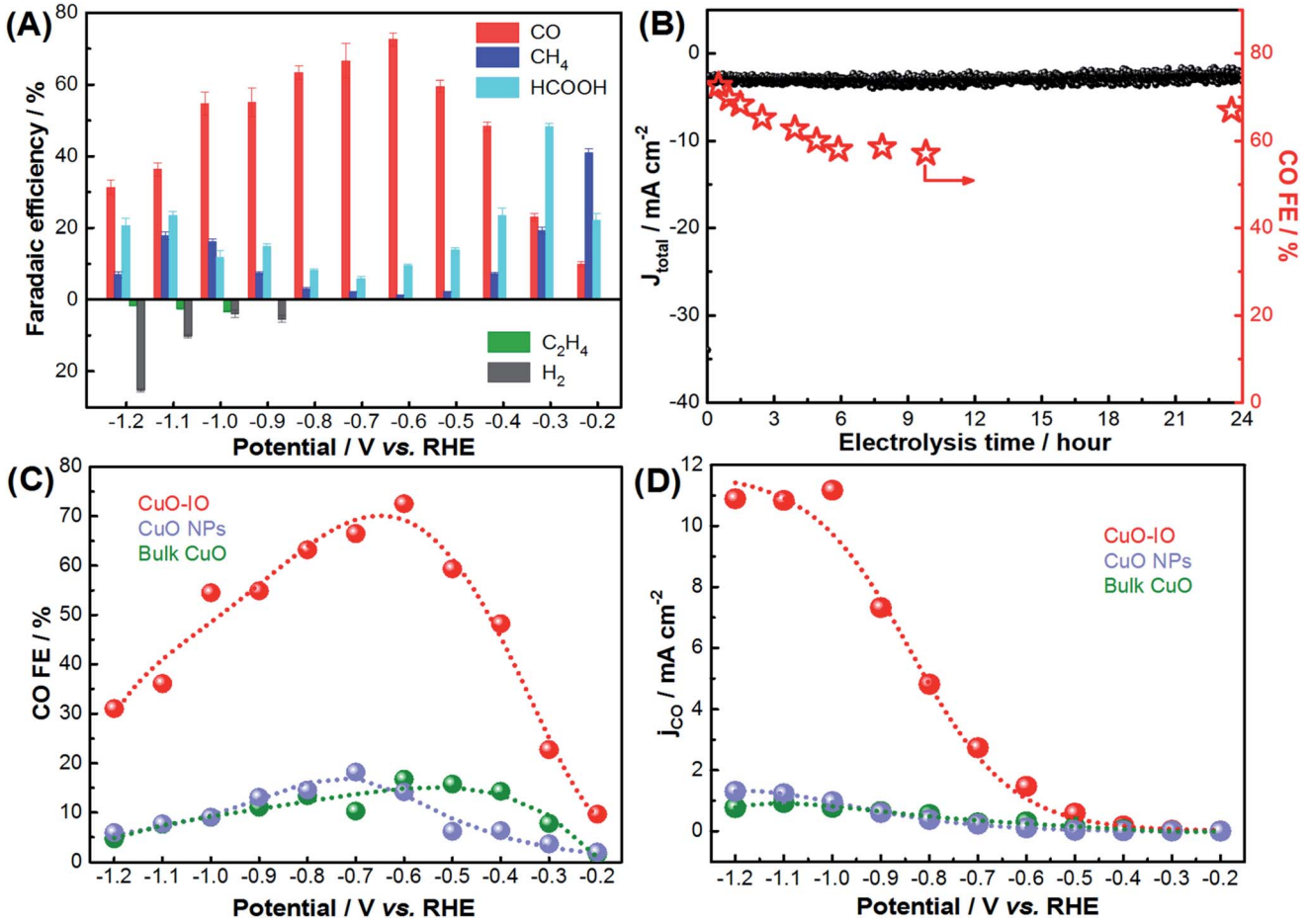

Fig. 2 (A) Potential-dependent faradaic efficiencies for CO_2 reduction products over CuO-IO catalyst in CO_2 saturated 0.1 M $KHCO_3$. (B) Long-term electrocatalytic performance of CuO-IO catalyst at −0.6 V *vs.* RHE. Comparisons of (C) CO faradaic efficiency (FE) and (D) CO partial current density (j_{CO}) at various negative potentials for CuO-IO, ~50 nm CuO NPs, and bulk CuO powder.

ESI†). The potential-dependent faradaic efficiencies for all products in Fig. S19 and S20 (ESI†) show that unlike CuO-IO, these more traditionally structured CuO catalysts produced mostly H_2 (FE ~ 50–70%) with small yields of CO (FE < 20%) at moderate negative potentials and ~20% FE of ethylene at high overpotentials. The product distribution obtained over these catalysts is similar to those of many copper catalysts reported before.[11,12,14,24,25,28] As shown in Fig. 2C, D and Fig. S21 (ESI†), the CuO-IO demonstrated substantially higher FEs and selectivities towards CO, and CO partial current density (j_{CO}) compared with the CuO NPs and bulk CuO catalysts. The 141 mV dec^{-1} Tafel slope for CO production at CuO-IO was close to the 120 mV dec^{-1} expected for a rate determining step involving the initial electron transfer to CO_2 (Fig. S22, ESI†).[10,13,26,29,31] Tafel slopes for the CuO NPs and bulk CuO were 178 and 184 mV dec^{-1}, respectively.

In situ measurements

The Pourbaix diagram for the Cu–H_2O system[38] indicates CuO should reduce to metallic Cu under EC-CO_2RR at potentials more negative than −0.5 V, which is consistent with the cyclic voltammogram (CV) of CuO-IO in CO_2 saturated 0.1 M $KHCO_3$ (Fig. 3A). The oxidation state of Cu-based catalysts during CO_2RR is still debated in the literature,[14,15,18,24,28,39,40] and we conducted *in situ* XAS, Raman spectroscopy, and XRD experiments to monitor the oxidation state, surface structure, crystallite size, and crystallographic orientation of CuO-IO under electrochemical potential control.

Cu K-edge XANES and EXAFS were collected at various potentials in CO_2 saturated 0.1 M $KHCO_3$. The EXAFS spectra in Fig. 3B shows the CuO-IO was in the Cu^{2+} oxidation state under open circuit. A reduction of the Cu–O and Cu–Cu scattering peaks of CuO at 1.53 Å and 2.52 Å, and the emergence of the first Cu–Cu coordination shell in metallic Cu at 2.21 Å indicate the onset of Cu-oxide reduction at an applied potential of −0.2 V *vs.* RHE.[14,15] These changes became more apparent with increasingly cathodic potentials, and comparison with the bulk Cu foil reference indicates near complete reduction beyond −0.6 V *vs.* RHE. These potential-dependent spectroscopic changes are consistent with the Cu-oxide reduction peak centered at approximately −0.45 V *vs.* RHE in Fig. 3A, and they agree with the Cu–H_2O Pourbaix diagram[38] and similar behavior recently reported by Velasco-Vélez *et al.*[40] The associated Cu K-edge

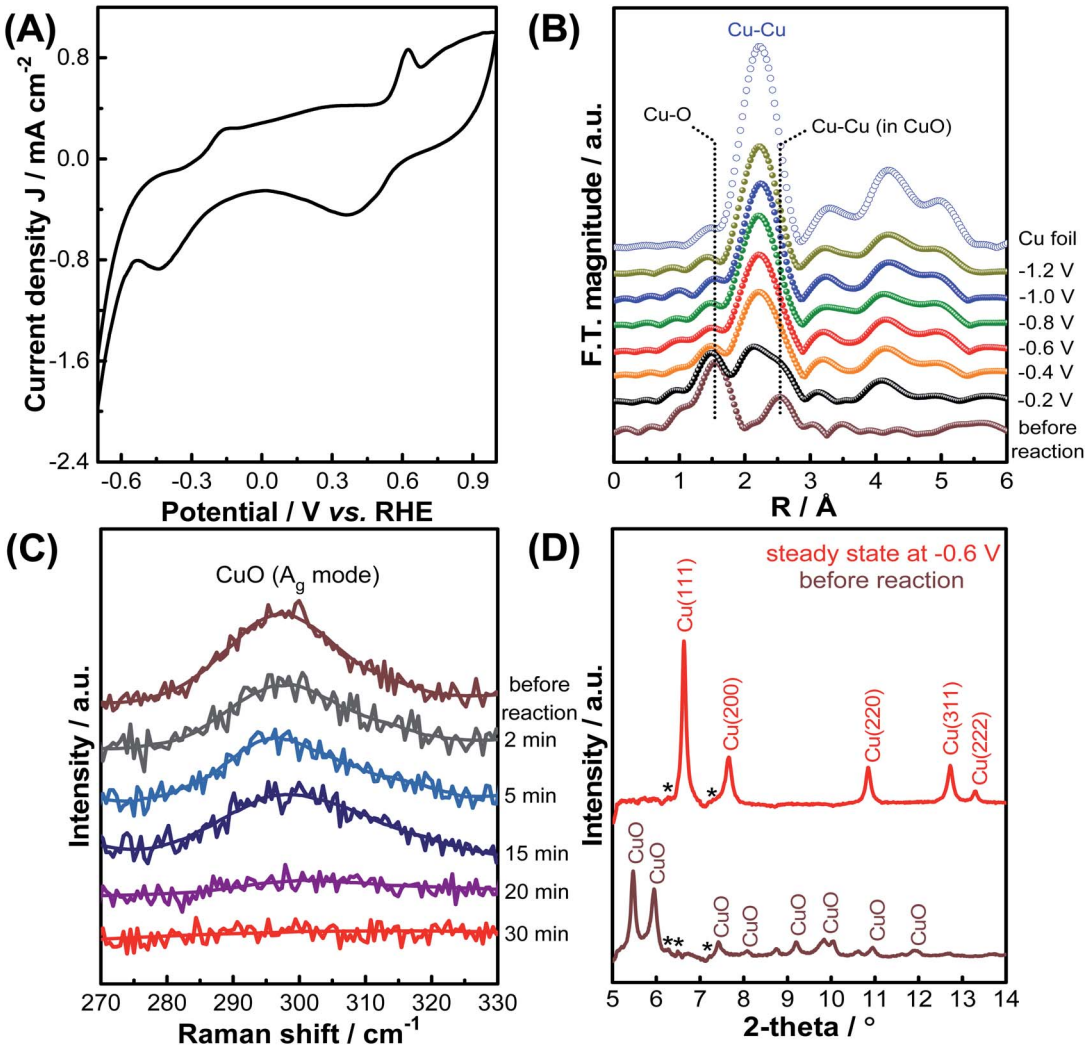

Fig. 3 (A) Cyclic voltammetry of fresh CuO-IO electrode in CO_2 saturated 0.1 M $KHCO_3$. (B) Potential-dependent k^2-weighted R-space EXAFS analysis (no phase correction) from −0.2 V to −1.2 V *vs.* RHE (collected at 30 min at each potential). (C) *In situ* Raman spectra for tracking surface structure of CuO-IO during EC-CO_2RR at −0.6 V (using 785 nm laser source). (D) SXRD patterns of CuO-IO electrode under open circuit and steady state at −0.6 V *vs.* RHE (*indicates residual carbon paper features and Kapton window from background subtraction).

XANES spectra collected at different potentials and while being held at −0.6 V are presented in Fig. S23 and S24 (ESI†).

XAS is a bulk technique, and some studies have suggested the presence of residual surface or sub-surface oxides during EC-CO_2RR that could impact EC-CO_2RR activity and selectivity.[8,14,15,18,24] To address this question, we also employed *in situ* Raman spectroscopy as a more surface sensitive technique to probe the surface structure changes of CuO-IO during the application of electrochemical potentials. *Ex situ* Raman spectrum in Fig. S25 (ESI†) shows three indicative A_g, B_{1g}, and B_{2g} modes for fresh CuO-IO electrode. As shown in Fig. 3C, we monitored the wavenumber region associated with the predominant A_g feature of CuO at 294 cm^{-1} to track oxidation state during CO_2RR. The spectrum collected before reaction is consistent with previous reports of CuO samples containing ~10 nm grain sizes recorded with a 782 nm laser.[41] This feature gradually disappeared during the application of at −0.6 V *vs.* RHE in CO_2-purged $KHCO_3$, and no other peaks associated with Cu_2O were found during the reaction in the region of 100–250 cm^{-1} and 330–600 cm^{-1}. Similar results were obtained at −0.8 V and −1.0 V *vs.* RHE (Fig. S26, ESI†). Metallic copper is Raman-inactive, and the immediate decrease in intensity and subsequent disappearance under electrocatalytic potentials strongly indicate the reduction of CuO into Cu^0 on the electrocatalyst surface. These results are also in good agreement with other previous reports of Cu-oxide reduction,[8,12,27,39] specifically, those of Ren[28] and Wang *et al.*[39] who attributed the disappearance of the A_g mode during the application of cathodic potentials to copper-oxide reduction and Cu^0 formation. Raman spectrum collected once the catalyst returned to open circuit showed the presence of mixed Cu_2O and CuO species (Fig. S27, ESI†), which reflects the reversibility of the Cu redox process.

Finally, *in situ* XRD were collected under open circuit and at −0.6 V *vs.* RHE to further probe the crystallographic orientation and crystallite size during EC-CO_2RR (Fig. 3D). CuO was

identified before reaction, which is consistent with both Cu K-edge XAS/EXAFS and Raman measurements. Under steady state operating conditions at −0.6 V *vs.* RHE, we found the presence of Cu (111), (200), (220), (311), and (222) peaks indicative of face-centered cubic Cu (space group $Fm\bar{3}m$), and we did not observe any significant signatures associated with oxides under working conditions (Fig. S24 and S28, ESI†). The results identify metallic copper with lattice constant $a = b = c = 3.6102$ Å and mean crystallite size of 10–11 nm during EC-CO_2RR, which is consistent with pre-reaction TEM analysis. The peak intensity ratio of Cu(111) to Cu(200) for an ideal polycrystalline Cu surface was reported to be *ca.* 3.03.[30] We have estimated that the average relative intensity ratio of Cu(111) and Cu(200) peaks at during EC-CO_2RR at −0.6 V *vs.* RHE is 3.58 (Fig. S28, ESI†), implying the dominance of closed-packed Cu(111) surface or preferential (111) orientation of the catalyst during the reaction. Importantly, we observed that the crystallographic orientation and crystallite size of operating catalyst did not substantially change during five hours of measurement at −0.6 V *vs.* RHE (Fig. S28, ESI†). Similar to Raman measurements, we also observed re-oxidation of the catalyst once it was returned to open circuit after the application of cathodic potential (Fig. S29, ESI†). Correlating these various *in situ* measurements strongly implies that Cu^0 with a preferred Cu(111) orientation is a dominant species present in the CuO-IO catalyst during EC-CO_2RR.

Discussion

The oxide-derived Cu-IO catalysts exhibited some of the highest CO_2-to-CO selectivity among several oxide-derived copper electrocatalysts at low to moderate overpotentials (Table S4, ESI†).[9,10,13,17,26–29,42] For example, both Kanan,[10] Ren[28] and their coworkers reported that oxide-derived copper catalysts with a relatively high surface roughness could achieve selective CO and/or HCOOH production at low overpotentials. Wang and coworkers[9,17,29] also achieved CO FEs around 60% between −0.3 V and −0.5 V *vs.* RHE using Cu_2O-derived copper nanowires with a surface containing small (<10 nm) crystallites, as well as oxide-derived, 3D copper nanostructures.

In the present study, the selective EC-CO_2RR performance and strong HER inhibition demonstrated by the CuO-IO catalyst may be attributed to both its 3D morphology and crystallographic surface orientation. The CuO-IO catalyst is composed of small nanoparticles arranged in a 3D interconnected porous structure that offers a large surface-to-volume ratio. The measured ECSA (2.96 cm^2) and RF (30.8) of CuO-IO were considerably larger than the ∼50 nm diameter CuO NPs and bulk CuO powder (0.37–0.55 cm^2 and RF = 5.3–7.8; Fig. S30 and Table S5, ESI†). The preferential Cu(111) surface/orientation is also expected to demonstrate higher C_1 selectivity due to weaker binding of *CO and *COOH intermediates, whereas Cu(100) facets have favored C_{2+} production owing to a lower energetic barrier for intermediate hydrogenation.[8,9,11,23,30,42–50]

In the low and moderate overpotential range (−0.2 to −0.8 V *vs.* RHE), the CuO-IO catalyst produced exclusive C_1 products and almost no H_2 evolution. In this potential range, the highly roughened, porous CuO-IO surface allowed rapid consumption of both CO_2 and H^+.[28,42] The observed current density likely increased the local pH sufficiently to reduce the number of protons available for HER,[42,51] while the Cu(111) orientation favored C_1 production over C_2 formation.[9,23,30,42,43,45,47,49,50]

In the high overpotential range, large current densities can increase the local pH at copper electrodes to 13 or higher.[42,43] These basic conditions can activate additional C_2 forming reaction pathways and deplete the concentration of available CO_2 molecules.[42,44,51,52] The effect of these two phenomena was observed beyond −0.8 V *vs.* RHE with increased H_2 evolution and the emergence of C_2 product formation at the CuO-IO catalyst. While we did observe hydrocarbon formation at large overpotentials, methane was substantially favored over ethylene. These results are largely consistent with the expected C_1 preference of Cu(111) facets.[9,23,30,42,43,45,47,49,50]

Previous works have proposed C_{2+} forming reaction pathways on Cu(111).[48,49] C_2H_4 formation can share the *COH pathway with CH_4 production, go through a *CHO pathway followed by C–C coupling, and/or undergo *CO dimerization.[12,15,16,23,27,42,43,48] Strong suppression of C_2 products along with favorable CH_4 formation at potentials beyond −0.9 V *vs.* RHE indicate that CuO-derived Cu-IO promotes either the CHO or COH pathway over CO dimerization. Our results are consistent with previous findings of preferential methane formation on Cu(111) at more elevated overpotentials over C_2 products.[42,43,45,47,49,50]

Finally, we can compare our results with others to identify the impact of Cu-IO pore size.[26,27] Cu-IO catalysts prepared by electrochemical deposition formed with larger diameter pores (340–600 nm) and contained larger, more bulk-like particles and crystallites.[26,27] Fig. S31 (ESI†) shows that increasing pore diameter from 180 nm (current study) to 600 nm decreased CO selectivity while increased both H_2 and C_2 production. Cu-IOs with larger crystallite size and pore diameter demonstrated product distributions similar to that of bulk CuO powder (Fig. S20, ESI†), suggesting both pore diameter and crystallite size may be a design principle for tuning catalyst selectivity.

Taken together, our results suggest the CuO-IO catalyst selectively produced CO owing to the synergy between the morphology and structure of the electrocatalyst. The 3D interconnected porous structure created pH gradients that decreased proton availability and suppressed HER, while the dominant Cu(111) orientation favored selective C_1 formation. Our work provides better understanding of the structure–property relationships of porous copper-based catalysts, and provides insight into the selective, precious-metal free reduction of CO_2 into CO at CuO-IO.

Conclusions

In summary, our hierarchical CuO-derived IO catalyst has shown impressive CO selectivity across a wide potential range with minor H_2 evolution. This performance is superior in faradaic efficiency (∼72.5%), selectivity (∼90%) and CO current density compared with other bulk and nanoparticulate copper oxide catalysts (FE < 20%). Our results have demonstrated the benefit

of 3D interconnected porous structure that promotes EC-CO_2RR by creating local pH gradients within the catalyst pores that deplete the local concentration of protons available for HER. In addition, the high surface roughness reduced copper surface, and Cu(111) oriented-surface facilitate a C_1 reaction path. In this regard, our work may provide more understanding on structure–property relation of oxide-derived copper catalyst for CO production from fossil fuel-generated CO_2 emission.

Disclaimer

This work was funded by the Department of Energy, National Energy Technology Laboratory, an agency of the United States Government, through a support contract with Leidos Research Support Team (LRST). Neither the United States Government nor any agency thereof, nor any of their employees, nor LRST, nor any of their employees, makes any warranty, expressed or implied, or assumes any legal liability or responsibility for the accuracy, completeness, or usefulness of any information, apparatus, product, or process disclosed, or represents that its use would not infringe privately owned rights. Reference herein to any specific commercial product, process, or service by trade name, trademark, manufacturer, or otherwise, does not necessarily constitute or imply its endorsement, recommendation, or favoring by the United States Government or any agency thereof. The views and opinions of authors expressed herein do not necessarily state or reflect those of the United States Government or any agency thereof.

Conflicts of interest

There are no conflicts to declare.

Acknowledgements

This work was performed in support of the US Department of Energy's Fossil Energy Crosscutting Technology Research Program. The Research was executed through the NETL Research and Innovation Center's CO_2 Utilization Technologies. Research performed by Leidos Research Support Team staff was conducted under the RSS contract 89243318CFE000003. This research used the 8-ID (ISS) and 23-ID-2 (IOS) beamlines of the National Synchrotron Light Source II, a U.S. Department of Energy (DOE) Office of Science User Facility operated for the DOE Office of Science by Brookhaven National Laboratory under Contract No. DE-SC0012704. This research used Beamline 17-BM of the Advanced Photon Source, a U.S. Department of Energy (DOE) Office of Science User Facility operated for the DOE Office of Science by Argonne National Laboratory under Contract No. DE-AC02-06CH11357. The authors acknowledge use of the Materials Characterization Facility at Carnegie Mellon University supported by grant MCF-677785. The authors also thank Dr William A. Rogers and Dr Bryan Hughes for *in situ* cell printing.

References

1 Q. Lu and F. Jiao, *Nano Energy*, 2016, **29**, 439–456.
2 Y. Terunuma, A. Saitoh and Y. Momose, *J. Electroanal. Chem.*, 1997, **434**, 69–75.
3 F. Studt, I. Sharafutdinov, F. Abild-Pedersen, C. F. Elkjær, J. S. Hummelshøj, S. Dahl, I. Chorkendorff and J. K. Nørskov, *Nat. Chem.*, 2014, **6**, 320–324.
4 A. S. Hall, Y. Yoon, A. Wuttig and Y. Surendranath, *J. Am. Chem. Soc.*, 2015, **137**, 14834–14837.
5 N. Sreekanth, M. A. Nazrulla, T. V. Vineesh, K. Sailaja and K. L. Phani, *Chem. Commun.*, 2015, **51**, 16061–16064.
6 Y. Yoon, A. S. Hall and Y. Surendranath, *Angew. Chem., Int. Ed.*, 2016, **55**, 15282–15286.
7 J.-H. Kim, H. Woo, J. Choi, H.-W. Jung and Y.-T. Kim, *ACS Catal.*, 2017, **7**, 2101–2106.
8 L. Mandal, K. R. Yang, M. R. Motapothula, D. Ren, P. Lobaccaro, A. Patra, M. Sherburne, V. S. Batista, B. S. Yeo, J. W. Ager, J. Martin and T. Venkatesan, *ACS Appl. Mater. Interfaces*, 2018, **10**, 8574–8584.
9 D. Raciti, K. J. Livi and C. Wang, *Nano Lett.*, 2015, **15**, 6829–6835.
10 C. W. Li and M. W. Kanan, *J. Am. Chem. Soc.*, 2012, **134**, 7231–7234.
11 R. Reske, H. Mistry, F. Behafarid, B. R. Cuenya and P. Strasser, *J. Am. Chem. Soc.*, 2014, **136**, 6978–6986.
12 D. Ren, Y. Deng, A. D. Handoko, C. S. Chen, S. Malkhandi and B. S. Yeo, *ACS Catal.*, 2015, **5**, 2814–2821.
13 M. Ma, K. Djanashvili and W. A. Smith, *Phys. Chem. Chem. Phys.*, 2015, **17**, 20861–20867.
14 H. Mistry, A. S. Varela, C. S. Bonifacio, I. Zegkinoglou, I. Sinev, Y.-W. Choi, K. Kisslinger, E. A. Stach, J. C. Yang, P. Strasser and B. R. Cuenya, *Nat. Commun.*, 2016, **7**, 12123.
15 A. Eilert, F. S. Roberts, D. Friebel and A. Nilsson, *J. Phys. Chem. Lett.*, 2016, **7**, 1466–1470.
16 C. Reller, R. Krause, E. Volkova, B. Schmid, S. Neubauer, A. Rucki, M. Schuster and G. Schmid, *Adv. Energy Mater.*, 2017, **7**, 1602114.
17 L. Cao, D. Raciti, C. Li, K. J. T. Livi, P. F. Rottmann, K. J. Hemker, T. Mueller and C. Wang, *ACS Catal.*, 2017, **7**, 8578–8587.
18 A. Eilert, F. Cavalca, F. S. Roberts, J. Osterwalder, C. Liu, M. Favaro, E. J. Crumlin, H. Ogasawara, D. Friebel, L. G. M. Pettersson and A. Nilsson, *J. Phys. Chem. Lett.*, 2017, **8**, 285–290.
19 W. Zhu, Y.-J. Zhang, H. Zhang, H. Lv, Q. Li, R. Michalsky, A. A. Peterson and S. Sun, *J. Am. Chem. Soc.*, 2014, **136**, 16132–16135.
20 K. Jiang, P. Kharel, Y. Peng, M. K. Gangishetty, H.-Y. G. Lin, E. Stavitski, K. Attenkofer and H. Wang, *ACS Sustainable Chem. Eng.*, 2017, **5**, 8529–8534.
21 V. R. Calderone, N. R. Shiju, D. C. Ferré and G. Rothenberg, *Green Chem.*, 2011, **13**, 1950–1959.
22 O. Martin, C. Mondelli, D. Curulla-Ferré, C. Drouilly, R. Hauert and J. Pérez-Ramírez, *ACS Catal.*, 2015, **5**, 5607–5616.
23 D. Raciti and C. Wang, *ACS Energy Lett.*, 2018, **3**, 1545–1556.
24 P. De Luna, R. Quintero-Bermudez, C.-T. Dinh, M. B. Ross, O. S. Bushuyev, P. Todorović, T. Regier, S. O. Kelley, P. Yang and E. H. Sargent, *Nat. Catal.*, 2018, **1**, 103–110.

25 H. S. Jeon, S. Kunze, F. Scholten and B. R. Cuenya, *ACS Catal.*, 2018, **8**, 531–535.
26 X. Zheng, J. Han, Y. Fu, Y. Deng, Y. Liu, Y. Yang, T. Wang and L. Zhang, *Nano Energy*, 2018, **48**, 93–100.
27 H. Song, M. Im, J. T. Song, J.-A. Lim, B.-S. Kim, Y. Kwon, S. Ryu and J. Oh, *Appl. Catal., B*, 2018, **232**, 391–396.
28 D. Ren, J. Fong and B. S. Yeo, *Nat. Commun.*, 2018, **9**, 925.
29 D. Raciti, Y. Wang, J. H. Park and C. Wang, *ACS Appl. Energy Mater.*, 2018, **1**, 2392–2398.
30 A. Dutta, M. Rahaman, N. C. Luedi, M. Mohos and P. Broekmann, *ACS Catal.*, 2016, **6**, 3804–3814.
31 Y. Yang, L. Ohnoutek, S. Ajmal, X. Zheng, Y. Feng, K. Li, T. Wang, Y. Deng, Y. Liu, D. Xu, V. K. Valev and L. Zhang, *J. Mater. Chem. A*, 2019, **7**, 11836–11846.
32 A. Stein, B. E. Wilson and S. G. Rudisill, *Chem. Soc. Rev.*, 2013, **42**, 2763–2803.
33 A. Wuttig and Y. Surendranath, *ACS Catal.*, 2015, **5**, 4479–4484.
34 D. H. Won, H. Shin, M. W. Chung, H. Jung, K. H. Chae, H.-S. Oh, Y. J. Hwang and B. K. Min, *Appl. Catal., B*, 2019, **258**, 117961.
35 B. Ravel and M. Newville, *J. Synchrotron Radiat.*, 2005, **12**, 537–541.
36 B. H. Toby and R. B. Von Dreele, *J. Appl. Crystallogr.*, 2013, **46**, 544–549.
37 E. L. Clark, J. Resasco, A. Landers, J. Lin, L.-T. Chung, A. Walton, C. Hahn, T. F. Jaramillo and A. T. Bell, *ACS Catal.*, 2018, **8**, 6560–6570.
38 B. Beverskog and I. Puigdomenech, *J. Electrochem. Soc.*, 1997, **144**, 3476–3483.
39 L. Wang, K. Gupta, J. B. M. Goodall, J. A. Darr and K. B. Holt, *Faraday Discuss.*, 2017, **197**, 517–532.
40 J.-J. Velasco-Vélez, T. Jones, D. Gao, E. Carbonio, R. Arrigo, C.-J. Hsu, Y.-C. Huang, C.-L. Dong, J.-M. Chen, J.-F. Lee, P. Strasser, B. R. Cuenya, R. Schlögl, A. Knop-Gericke and C.-H. Chuang, *ACS Sustainable Chem. Eng.*, 2019, **7**, 1485–1492.
41 J. F. Xu, W. Ji, Z. X. Shen, W. S. Li, S. H. Tang, X. R. Ye, D. Z. Jia and X. Q. Xi, *J. Raman Spectrosc.*, 1999, **30**, 413–415.
42 D. Raciti, M. Mao, J. H. Park and C. Wang, *J. Electrochem. Soc.*, 2018, **165**, F799–F804.
43 K. J. P. Schouten, Z. Qin, E. P. Gallent and M. T. M. Koper, *J. Am. Chem. Soc.*, 2012, **134**, 9864–9867.
44 Y. Hori, I. Takahashi, O. Koga and N. Hoshi, *J. Mol. Catal. A: Chem.*, 2003, **199**, 39–47.
45 Y. Lum, B. Yue, P. Lobaccaro, A. T. Bell and J. W. Ager, *J. Phys. Chem. C*, 2017, **121**, 14191–14203.
46 A. Bagger, W. Ju, A. S. Varela, P. Strasser and J. Rossmeisl, *ACS Catal.*, 2019, **9**, 7894–7899.
47 M. Gattrell, N. Gupta and A. Co, *J. Electroanal. Chem.*, 2006, **594**, 1–19.
48 X. Nie, W. Luo, M. J. Janik and A. Asthagiri, *J. Catal.*, 2014, **312**, 108–122.
49 C. Hahn, T. Hatsukade, Y.-G. Kim, A. Vailionis, J. H. Baricuatro, D. C. Higgins, S. A. Nitopi, M. P. Soriaga and T. F. Jaramillo, *Proc. Natl. Acad. Sci. U. S. A.*, 2017, **114**, 5918–5923.
50 A. A. Peterson, F. Abild-Pedersen, F. Studt, J. Rossmeisl and J. K. Norskov, *Energy Environ. Sci.*, 2010, **3**, 1311–1315.
51 M. R. Singh, E. L. Clark and A. T. Bell, *Phys. Chem. Chem. Phys.*, 2015, **17**, 18924–18936.
52 A. S. Varela, M. Kroschel, T. Reier and P. Strasser, *Catal. Today*, 2016, **260**, 8–13.

